Inverse-Designed Non-Uniform Silicon Nitride Gratings With High Beam Steering Performance

Tianyang Fu, Ziwei Ma, Xin Yan, Xia Zhang, and Xiaomin Ren

***Abstract*—Non-uniform silicon nitride grating antennas are designed by inverse-design method. In the wavelength range of 1500-1590 nm, the non-uniform gratings exhibit a large scanning range of 13.2° and high wavelength tuning efficiency of 0.147 °/nm, nearly 2.4 times that of the uniform gratings, along with superior transmission and directionality performance. At 1550 nm, a high side mode suppression ratio of 4.32 dB is obtained for the non-uniform gratings, much higher than that of the uniform gratings (1.00 dB). This work may pave the way for the development of silicon nitride-based miniaturized optical phased arrays with excellent beam steering performance.**

***Index Terms*—Inverse design, silicon nitride, beam steering.**

I. Introduction

With the rapid development of autonomous driving and remote sensing technologies, light detection and ranging (Lidar) has attracted increasing attention for the advantages of large scanning angle range and high resolution [1], [2]. Lidars can be mainly divided into mechanical lidars, micro-electro-mechanical system (MEMS), flash, optical phased array (OPA), etc. Compared with other types of lidars, OPAs [3], [4], [5], [6], [7], [8] have attracted wide attention due to their low power consumption, small size and excellent performance. Besides, OPAs can be integrated with other optical components on a photonic chip, which is expected to significantly improve the reliability and anti-interference. Therefore, integrated optical OPAs are considered as one of the most potential solutions for miniaturized lidars.

OPA integration has been explored on various photonic platforms, of which silicon is particularly attractive due to its complementary metal-oxide semiconductor processes (CMOS) compatibility and high refractive index contrast [7], [9]. However, silicon-based devices are usually limited by the nonlinear loss incurred by the generation of carriers and two-photon absorption (TPA) effect [10], [11]. In recent years, silicon nitride has become a research hotspot in integrated photonics area. Compared with silicon, the weak nonlinear losses of silicon nitride allow the devices to work at higher optical powers. Besides, its lower refractive index contrast ($n_{SiN}\sim2$, $n_{SiO2}\sim1.5$, $n_{Si}\sim3.4$) results in higher tolerance than silicon during fabrication. Its low index contrast between usual substrate and cladding materials reduces the severity of any phase error arising from fabrication imperfections, decreases optical mode confinement and increases inter-waveguide coupling [12]. In addition, silicon nitride is transparent in the visible wavelength range and silicon nitride waveguides are standard in integrated photonics [12], [13], [14]. Due to the excellent optical waveguide properties, silicon nitride gratings have recently been designed and experimentally demonstrated for OPAs [15], [16], [17], [18], and the researches on directionality and beam steering efficiency have been carried out [19]. However, the beam steering ability, particularly the scanning range of current silicon nitride gratings is relatively poor, limiting their applications in high performance lidars.

At present, wavelength modulation beam steering in the longitudinal direction is generally based on periodic uniform gratings [20], which, however, are probably not the optimal structures for OPA applications. For example, studies have shown that sparse aperiodic waveguide arrays exhibited improved beam width and sidelobe suppression, with a smaller size [21], [22]. A four-period gratings also showed much larger scanning range and wavelength tuning efficiency in comparison with the single-period gratings [23]. Therefore, non-uniform aperiodic gratings may provide an effective way for the development of ultra-compact high-performance OPAs. However, it's difficult to obtain the optimal non-uniform grating structures in an infinite structural parameter space based on traditional design methods. In recent years, inverse design has gained increasing attention due to its potential in the design of ultra-compact high-performance optical devices. This approach combines optimization with electromagnetic calculation, which is able to find optimal structure in infinite parameter space to reach the performance goal. Up to date, a great deal of optical devices, such as polarization beam splitters [24], optical logical gates [25], optical varifocal mentalens [26], and optical waveguide crossings [27], have been demonstrated by inverse design method. However, up to date, inverse-designed silicon nitride gratings for beam steering have not been reported yet.

In this work, direct binary search (DBS)-based inverse design algorithm is used to design non-uniform silicon nitride grating antennas towards large-scanning-range OPAs. In the wavelength

Manuscript received 18 November 2022; revised 22 February 2023; accepted 21 March 2023. Date of publication 24 March 2023; date of current version 29 March 2023. This work was supported in part by the National Natural Science Foundation of China under Grant 61935003 and in part by the Fund of State Key Laboratory of Information Photonics and Optical Communications (Beijing University of Posts and Telecommunications), P. R. China under Grants IPOC2022ZZ01, IPOC2022ZT02, and IPOC2020ZZ01. *(Tianyang Fu and Ziwei Ma contributed equally to this work.) (Corresponding author: Xin Yan.)*

The authors are with the State Key Laboratory of Information Photonics and Optical Communications, School of Electronic Engineering, Beijing University of Posts and Telecommunications, Beijing 100876, China (e-mail: fty@bupt.edu.cn; vera_mzw@bupt.edu.cn; xyan@bupt.edu.cn; xzhang@bupt.edu.cn; xmren@bupt.edu.cn).

Digital Object Identifier 10.1109/JPHOT.2023.3261446

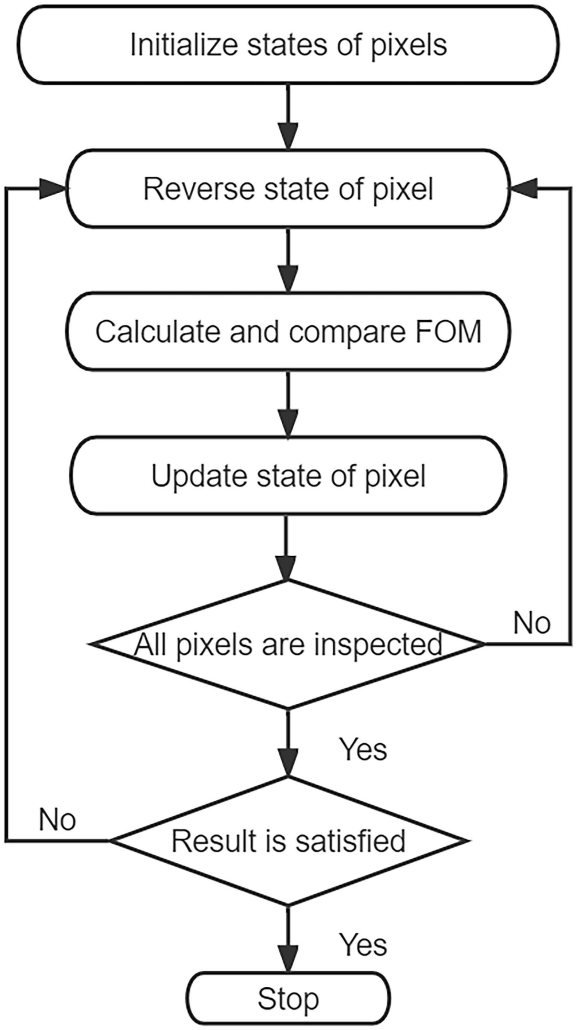

Fig. 1. Flow chart of DBS algorithm.

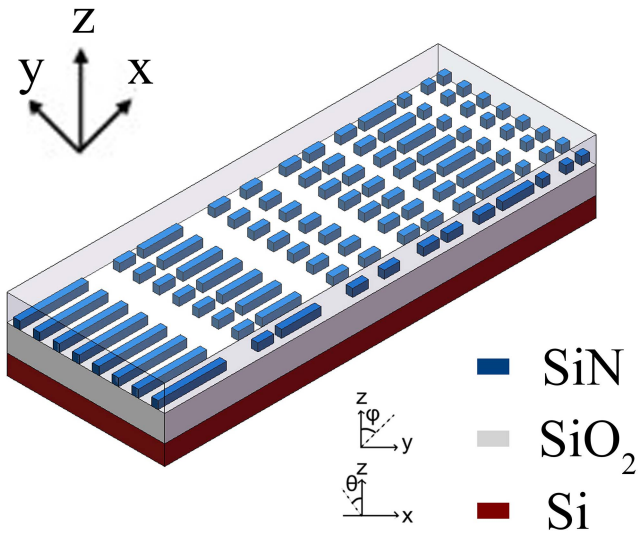

Fig. 2. Structure of proposed non-uniform silicon nitride grating antennas.

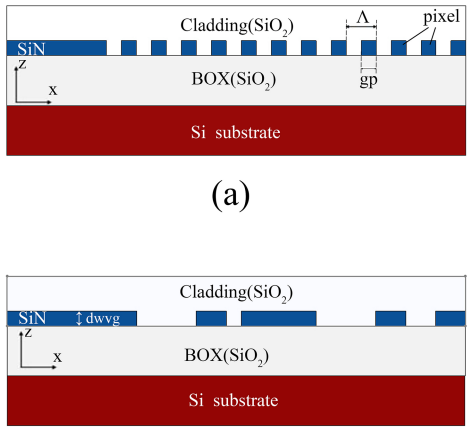

Fig. 3. Cross-section of (a) local part of optimized non-uniform gratings and (b) uniform gratings.

range of 1500-1590 nm, the scanning range and beam steering efficiency for non-uniform gratings reach 13.2° and 0.147 °/nm, respectively, nearly 2.4 times that of the uniform gratings. Meanwhile, non-uniform grating antennas exhibit good transmission and directionality. Besides, at 1550 nm, a high side mode suppression ratio (SMSR) of 4.32 dB is obtained for the non-uniform gratings over four times as that of the uniform gratings. This work demonstrates the potential of inverse design method in the design of silicon nitride-based miniaturized high-performance optical phased arrays.

II. Design and Simulation

The DBS algorithm flow chart is shown in Fig. 1. The design area is a N × M pixel array. Square pixels have two states including "presence" and "absence", which are represented by "1" and "0", respectively. Figure-of-merit (FOM) is used for evaluating the performance of designed structure. In a representative design process, pixels can be either initialized randomly or specified manually firstly, and an initial FOM can be calculated for comparison. Then randomly select one starting pixel and reverse its state. If the pixel's initial state is "1", switch its state to "0" and vice versa. After that, carry on an electromagnetic simulation based on the new structure to calculate a new FOM value corresponding to current structure. If the new FOM is better than the initial FOM, then update the structure by saving the new pixel state. If not, the chosen pixel's state will be restored. After the chosen pixel's state is determined, same optimization steps are carried out for the next pixel. The algorithm optimizes all pixels in the design area, and one iteration ends when all pixels have been inspected. Each iteration in the DBS algorithm will obtain a best FOM value. When FOM does not change any more, the optimizing program stops and the saved states of pixels are the optimal structure obtained [24], [28].

The proposed non-uniform silicon nitride grating antennas are shown in Fig. 2 (three-dimensional) and Fig. 3(a) (2-dimentional cross-section). The grating array consists of a silicon substrate,

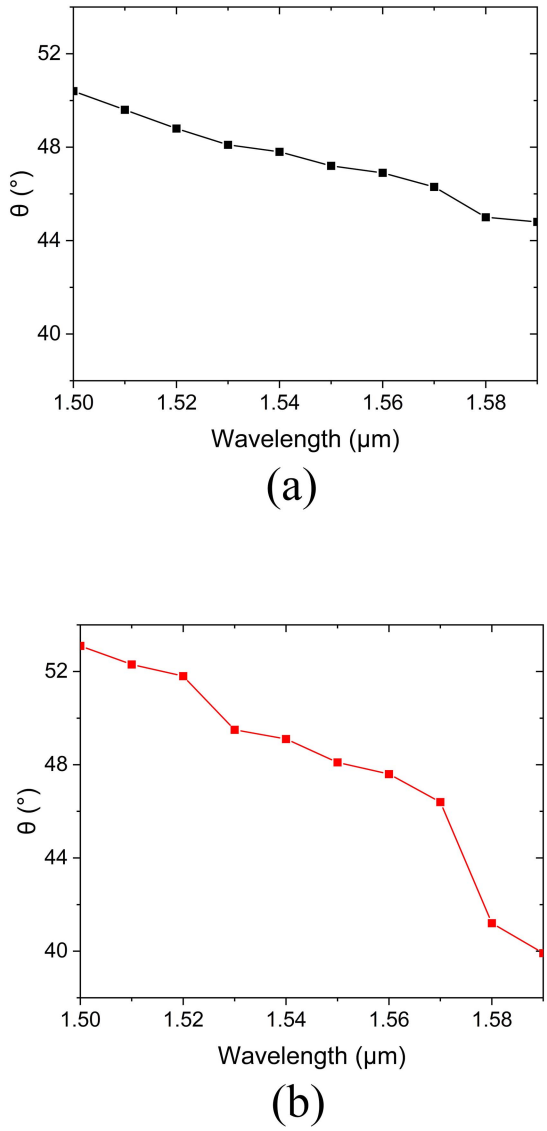

Fig. 4. Scanning angles of (a) uniform grating and (b) non-uniformly distributed grating in the longitudinal direction.

buried oxide (BOX) layer, upper cladding, and eight identical non-uniform silicon nitride gratings along y-direction. The width of gratings is fixed at 0.5 μm. The silicon nitride waveguides are separated by silicon dioxide layers, and non-uniform waveguide gratings have the same structure. The distance between adjacent waveguides is set to 1.5 μm. The design area on each grating antenna consists of 1 $\times$ 200 pixels. The pixel is 0.6 μm high, 0.5 μm wide and 0.6 μm long. Pixels are cubes made of either silicon nitride (state "1") or silicon dioxide (state "0"). In the longitudinal direction of non-uniform gratings, the beam steering angle is defined as θ, and the beam steering angle is defined as Φ in the lateral direction of non-uniform gratings. Before the optimization program starts, a randomly generated array initializes states of all pixels in the design area. That is, the material of all pixels is randomly set to silicon dioxide or silicon nitride. Then optimization begins. Each and every pixel switch state one by one and the newly obtained FOM value is compared

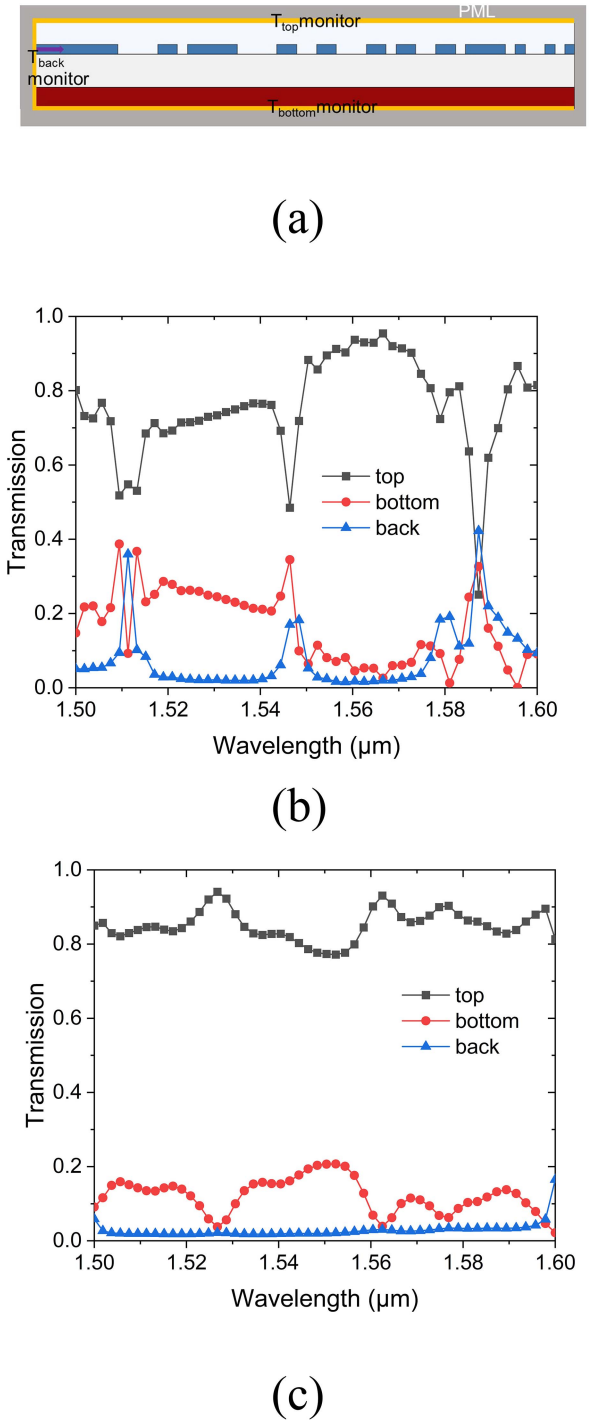

Fig. 5. (a) Simulation area for calculating transmission spectrum. (b) Transmission of uniform gratings. (c) Transmission of non-uniform gratings.

with previous FOM. If the new FOM value is better than the FOM value corresponding to previous structure, the new state of the pixel is retained. If the new FOM shows no improvement, then the pixel's state will change back. There are 200 pixels in the design area, hence the FOM value is calculated and compared 200 times in each iteration to obtain an optimal structure. For comparison, a uniform silicon nitride grating antenna is also studied, as plotted in Fig. 3(b). The grating period (Λ) is set to

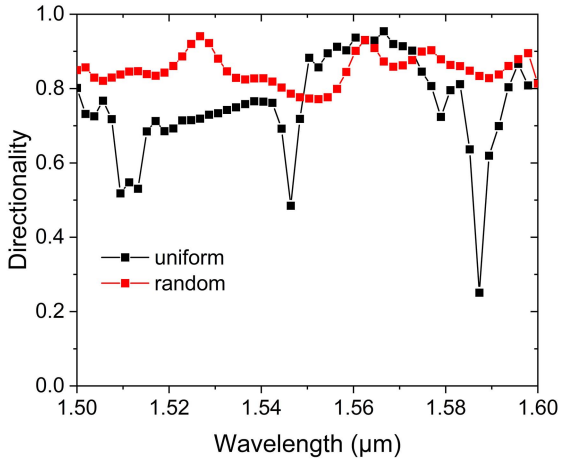

Fig. 6. Directionality of uniform and non-uniform gratings.

1.2 μm and the duty cycle is 0.5. The height of pixels (d_{wvg}) is set to 0.6 μm and the length of pixels (g_{p}) is fixed at 0.6 μm.

MEEP, an open-source finite difference time domain (FDTD) solver, is used to simulate the full 3D geometry of our design [29]. Formulas of 3D-FDTD method are directly derived from MaxWell's equations with the help of 3-D Yee's mesh. Perfectly matched layers (PMLs) are also imposed at the edges of the computational window. An eigenmode source is set as the input light source at the end of each waveguide, and TE polarization mode light is emitted into air by grating antennas. The refractive indices of silicon, silicon nitride and silicon dioxide at 1550 nm are 3.46, 1.99 and 1.45, respectively [24], [30]. Through 3D-FDTD method, the far-field patterns of beam steering can be obtained. Incident light is emitted in the air by the designed grating antennas, then the light beams can be detected in the far field and scanning angles can be measured, which can be used to assess the performance of designed structure.

III. Results and Discussion

Here, the *FOM* value of the algorithm is set as the scanning angle of the grating antenna between 1500-1590 nm, which is defined as

$$FOM = \theta_{\max} - \theta_{\min} \tag{1}$$

where $\theta_{\max}$ and $\theta_{\min}$ are the maximum and minimum longitudinal scan angle, respectively. The dependences of longitudinal scanning angles of uniform and non-uniform gratings on wavelength are shown in Fig. 4(a) and (b), respectively. As the wavelength switches from 1500 nm to 1590 nm, the scanning angle of uniform gratings for the TE polarization mode changes from 50.4° to 44.8°, resulting in a small scanning angle range of 5.6° and low wavelength tuning efficiency of 0.062 °/nm. While for the non-uniform gratings, in the same wavelength range from 1500 nm to 1590 nm, a larger scanning angle range of 13.2° is obtained, corresponding to a high wavelength tuning efficiency of 0.147 °/nm. The results demonstrate that compared with the uniform gratings, the non-uniform gratings can significantly increase the longitudinal scanning angle range. The physical mechanism that expands the wavelength tuning efficiency is to adjust the position of far-field beam by controlling the near-field of non-uniform gratings. For the non-uniform gratings, each pixel on a grating can be regarded as a light emitter correspond to different phases. Different emitters with different positions correspond to different optical paths. Therefore, emitters with different phases are generated by different optical paths. By changing the position of these pixels with DBS algorithm, the phases of the emitters are adjusted to control the near field of the gratings. The beam steering angle of an OPA is adjusted by controlling the phase and/or amplitude of emitters in the array. The electro-magnetic field close to the emitters, i.e., the near field, can be fully controlled. The far field is described by Fraunhofer diffraction theory and is basically the complex Fourier transform of the near field [31]. By controlling the near field, it is possible to manipulate the beam steering angle of grating antennas at far field, and the beam steering angle corresponding to different wavelengths can be measured at far field. Then the scanning angle in the wavelength range of 1500-1590 nm can be calculated using the angles measured at the far field.

Two-dimensional simulation method is adopted to investigate the antenna transmission and directionality, which is shown in Fig. 5(a). The transmission spectra of non-uniform grating antennas are computed in the simulation area. In the simulation area surrounded by PML, a non-uniform grating is set up on substrates and its material is silicon nitride. Source is fixed at the end of waveguide to input light power. A monitor, which is placed above waveguides, is used for computing "top" flux spectra (T_{top}). Also, there is a monitor below substrates to record "bottom" flux spectra (T_{bottom}). The monitor for T_{back} was placed on the left side as shown in Fig. 5(a).

In order to elaborate on how the transmission spectrums are obtained, it is necessary to explain how MEEP calculates transmission automatically. The computation involves keeping track of the fields and their Fourier transform in a certain region, and accumulate the Fourier transforms $\mathrm{E}_{\omega}(\mathrm{x})$ and $\mathrm{H}_{\omega}(\mathrm{x})$. Typically, getting transmission spectrum needs to run the simulation twice: once with only the incident wave and no scattering structure, and once with the scattering structure. The simulation with no scattering structure is used for normalization [29].

In order to calculate transmission spectrum, the first simulation with no scattering structure began and the incident power was calculated. Then a second simulation with non-uniform gratings calculated transmitted power. At last, normalize the transmitted flux of non-uniform gratings by the incident power to obtain transmission spectra. It should be noted that it gets a little more complicated when computing the "back" transmission spectrum, because it is necessary to separate incident power and reflected power. When calculating the reflected light power, be sure to subtracts the incident fields from the scattered fields before normalization. In this way the "back" transmission spectrum was obtained as well.

The transmission results are plotted in Fig. 5(b) and (c). The transmission spectrum in the upward direction is noted as "top", while the downstream transmission is represented by the "bottom" spectrum. Besides, the light power reflected back to the input waveguide is marked by the "back" spectrum. Fig. 5(b)

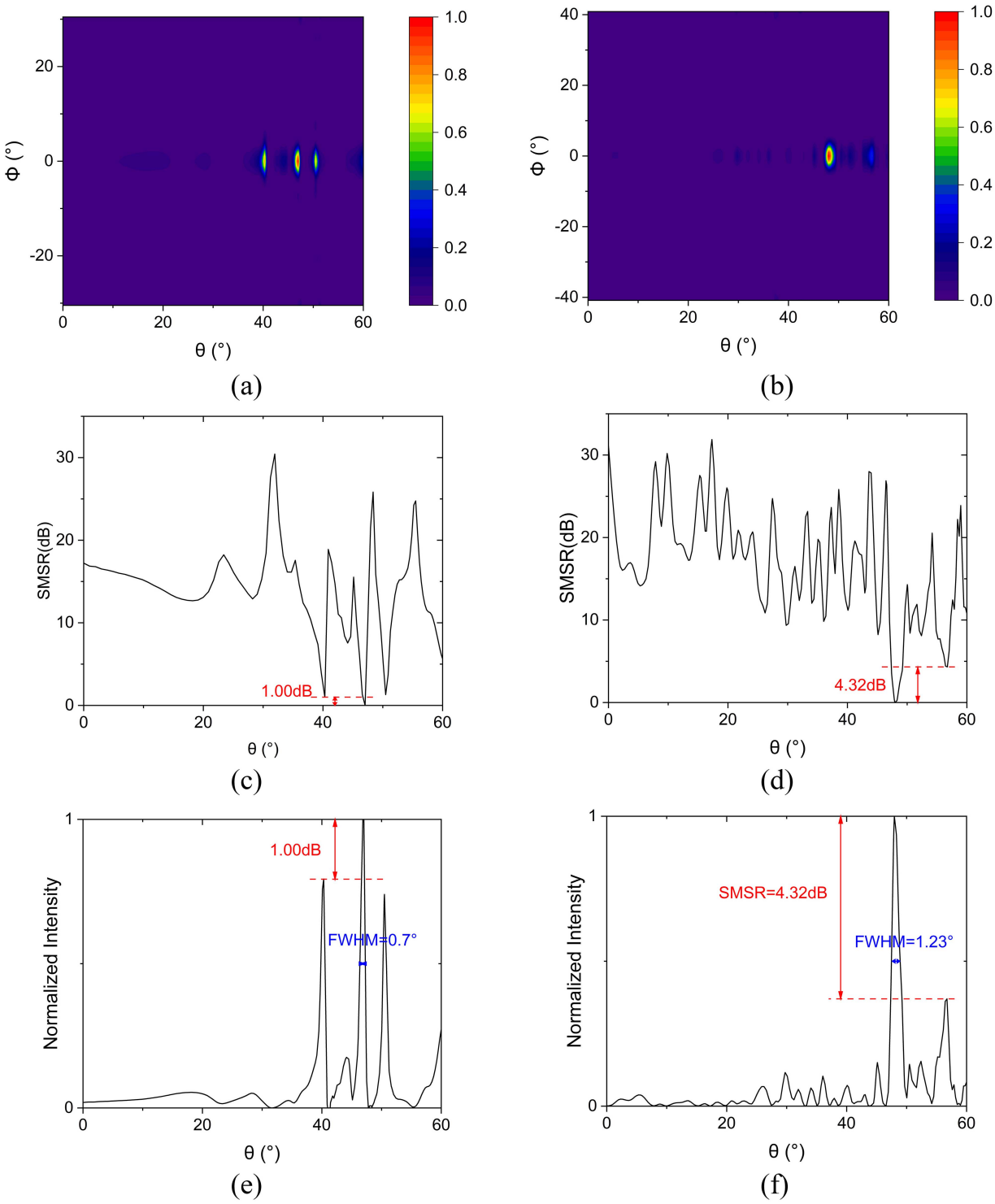

Fig. 7. Far-field distribution of (a) uniform gratings and (b) non-uniform gratings at 1550 nm. (c) SMSR of uniform gratings in log scale. (d) SMSR of non-uniform gratings in log scale. (e) Extracted and normalized far-field distributions of uniform gratings. (f) Extracted and normalized far-field distributions of non-uniform gratings.

shows the transmission spectrums of uniform grating antenna in three different directions. In most cases the transmission is over 70%. Particularly, three transmission valleys are observed at 1510 nm, 1546 nm and 1587 nm, corresponding to the photonic band gaps of the grating structure [32]. For uniform grating antennas, the light power reflected back to input waveguides increases at band gap and peak values appear, which is consistent to the transmission spectrum of upward direction ("top"). Except those peak values, the light power reflected back to the input waveguide is generally below 10% in the wavelength range of

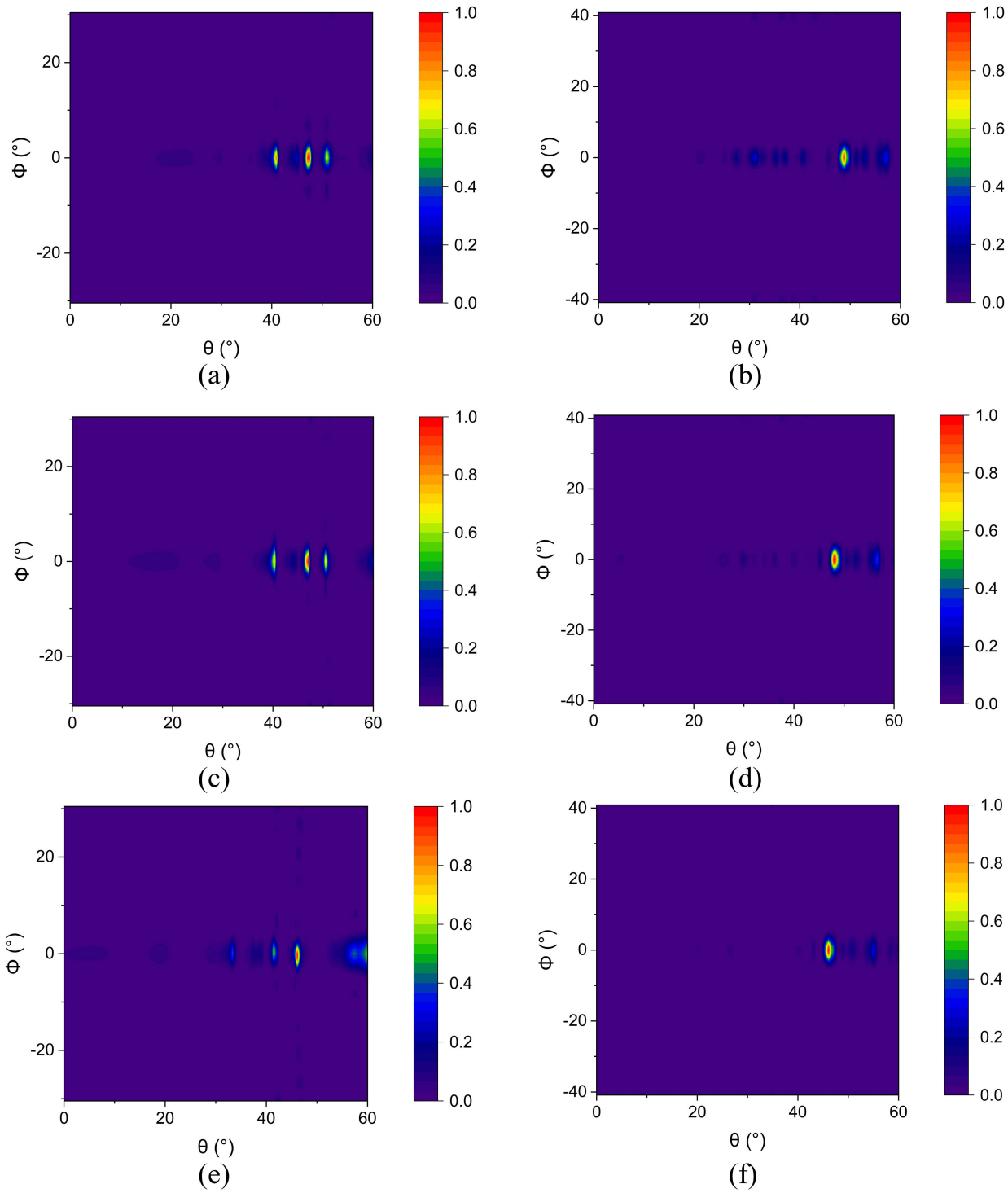

Fig. 8. Far-field distribution for (a) uniform gratings at 1530 nm. (b) Non-uniform gratings at 1530 nm. (c) Uniform gratings at 1550 nm. (d) Non-uniform gratings at 1550 nm. (e) Uniform gratings at 1570 nm. (f) Non-uniform gratings at 1570 nm.

1.50-1.58 μm. From 1. 58 to 1.60 μm, the "back" transmission rises slightly, but basically it can be kept below 20%. Fig. 5(c) shows the transmission spectrums of non-uniform grating antenna. The transmission in the upward direction is higher than 75% in the whole wavelength range of 1500 nm-1600 nm. The downward transmission and power reflected in the back direction are lower than 20% and 10%, respectively. Moreover, no obvious peaks and valleys are observed in the transmission spectra, as the non-uniform gratings break the periodic grating structure, eliminating the optical band gap effect.

Fig. 6 shows the directionality of uniform and non-uniform grating antennas, which can be used for measuring the light

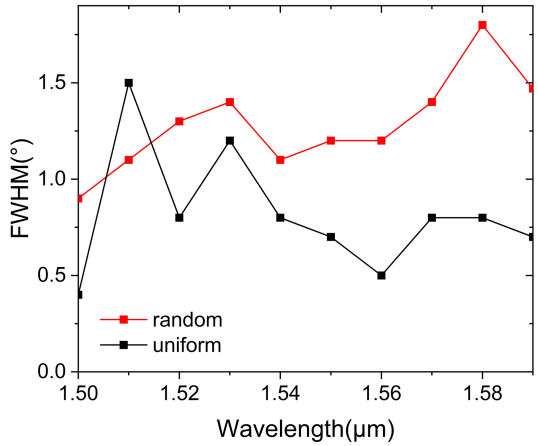

Fig. 9. Beam width variation of uniform and non-uniform gratings.

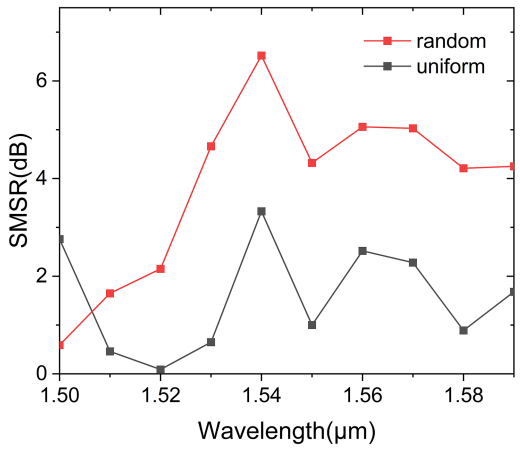

Fig. 10. SMSR of uniform and non-uniform gratings.

power emitted in the upward direction. The directionality of non-uniform grating antennas is defined as the ratio of "top" transmission to the total out-coupled power. According to Fig. 5(a), total out-coupled power includes upstream transmission (+z direction), downstream transmission (-z direction) and light that reflects back to the input waveguide (-x direction). The light that propagates in the forward direction along x remains in the waveguide, which can't be considered as "out-coupled" power [18], [32]. The larger the directionality is, the more energy the gratings emit upward, and the less energy loses and transmitted in other directions. The upstream transmission T_{top}, the downstream transmission T_{bottom}, and the reverse transmission T_{back}, which is defined as reflected light power back to the input waveguide, are used for evaluating the directionality of grating antennas. The following equation is used for characterizing the transmission directionality of the antenna [32]:

$$Directionality = T_{top}/\left(T_{bottom} + T_{top} + T_{back}\right) . \quad (2)$$

It can be seen from the equation that directionality is closely related to the transmission spectrum, hence the directionality spectrum is slightly similar to the transmission spectrum. From 1500 to 1600 nm, the non-uniform gratings show a relatively flat and high directionality over 77%, with a maximum value of 94% at 1526 nm. For the uniform gratings, the directionality is lower than that of the non-uniform structures at most wavelengths, particularly at short wavelengths. Similar to the transmission spectra, three valleys are also observed in the directionality curve, and a minimum value of 25% is obtained at 1587 nm. Hence, the non-uniform gratings show superior directionality performance in both amplitude and stability.

The far-field distribution at 1550 nm of the uniform and non-uniform gratings are plotted in Fig. 7(a) and (b), respectively. θ represents the beam steering angle in the longitudinal direction of non-uniform waveguide gratings, and Φ is the beam steering angle in the lateral direction, as is shown in Fig. 2. It can be seen clearly that the uniform gratings have two obvious large lobes, which are not observed in non-uniform structures.

The side mode suppression ratio (SMSR) is defined as

$$\mathrm{SMSR} = 10\log\left(I_{main}/I_{side}\right) \quad (3)$$

where I_{main} and I_{side} are the intensities of the main lobe and the side lobe, respectively. Fig. 7(c) shows SMSR of uniform gratings in log scale at 1550 nm where the transverse angle is zero, i.e., $\varphi = 0°$. SMSR of non-uniform gratings at 1550 nm is plotted in Fig. 7(d) where the transverse angle is zero. SMSR of the non-uniform gratings is 4.32 dB at 1550 nm, much higher than that of uniform structures (1.00 dB). In order to show the beam width directly, extracted and normalized far-field distributions at 1550 nm are also plotted in Fig. 7(e) and (f). The beam width of uniform and non-uniform gratings in θ direction is 0.7° and 1.23°, respectively. The beam width in the longitudinal direction mainly depends on the number of pixels. If the length of grating and the number of pixels on the waveguides increase, the beam width can be further reduced in longitudinal directions. Additionally, the beam power of uniform gratings in the main lobe is 21.35%, while non-uniform grating antennas concentrate 40.99% of light power, improved by 91.99%.

For comparison, Fig. 8 shows the far-field distribution of other wavelengths. Fig. 8(a) shows the far-field distribution of uniform gratings at 1530 nm. The beam width in θ direction is 1.2° and SMSR is 0.65 dB. Fig. 8(b) shows the far-field distribution of non-uniform gratings at 1530 nm. The beam width in θ direction is 1.4° and SMSR is 4.66 dB. Fig. 8(c) and (d) show the far-field distribution of uniform gratings and non-uniform gratings at 1550 nm, respectively. For uniform gratings, the beam width in θ direction is 0.7° and SMSR is 1.00 dB. For non-uniform gratings at 1550 nm, the beam width is 1.23° and SMSR is 4.32 dB. Fig. 8(e) shows the far-field distribution of uniform gratings at 1570 nm with a beam width of 0.8° and SMSR of 2.28 dB. Fig. 8(f) shows the far-field distribution of non-uniform gratings at 1570 nm. The beam width in θ direction is 1.4° and SMSR is 5.03 dB.

To judge the quality of the output beam, the beam width variation and SMSR have been calculated, as shown in Figs. 9 and 10. It can be seen from Fig. 9 that the beam width deviation in the θ direction can be kept less than 1° from 1500 to 1590 nm, and the widest beam is no more than 2° at 1580 nm. Besides, the SMSR of non-uniform gratings has also been improved over a broad wavelength range from 1510 to 1590 nm.

V. Conclusion

Non-uniform silicon nitride grating antennas are designed by DBS-based inverse design method. Compared with the uniform gratings, the non-uniform structures exhibit larger scanning range and improved optical beam quality. In the wavelength range of 1500–1590 nm, non-uniform gratings exhibit a scanning angle of 13.2° and beam steering efficiency of 0.147°/nm, 2.4 times that of the uniform gratings, along with superior transmission and directionality performance. At 1550 nm, a high *SMSR* of 4.32 dB is obtained for the non-uniform gratings, much higher than that of the uniform gratings. Additionally, non-uniform grating antennas show good performance in beam width and the SMSR is improved in most cases. This work demonstrates the potential of inverse design method in the development of miniaturized high-performance OPAs.

References

[1] C. V. Poulton et al., "High performance integrated optical phased arrays for chip-scale beam steering and LiDAR," in *Proc. Conf. Laser Electro-Opt. Appl. Technol.*, 2018, Paper ATu3R.2.

[2] S. A. Miller et al., "512-element actively steered silicon phased array for low-power LiDAR," in *Proc. Conf. Laser Electro-Opt. Appl. Technol.*, 2018, Paper JTh5C.2.

[3] S. Chung, H. Abediasl, and H. Hashemi, "A monolithically integrated large-scale optical phased array in silicon-on-insulator CMOS," *IEEE J. Solid-State Circuits*, vol. 53, no. 1, pp. 275–296, Jan. 2018, doi: 10.1109/JSSC.2017.2757009.

[4] J. K. Doylend, M. J. R. Heck, J. T. Bovington, J. D. Peters, and J. E. Bowers, "Free-space beam steering using silicon waveguide surface gratings," in *Proc. IEEE Photon. Soc. Annu. Meeting*, 2011, pp. 547–548.

[5] A. Hosseini et al., "On the fabrication of three-dimensional silicon-on-insulator based optical phased array for agile and large angle laser beam steering systems," *J. Vac. Sci. Technol. B*, vol. 28, no. 6, pp. C6O1–C6O7, Nov. 2010, doi: 10.1116/1.3511508.

[6] J. C. Hulme et al., "Fully integrated hybrid silicon two dimensional beam scanner," *Opt. Exp.*, vol. 23, no. 5, pp. 5861–5874, Mar. 2015, doi: 10.1364/OE.23.005861.

[7] C. V. Poulton et al., "Large-scale silicon nitride nanophotonic phased arrays at infrared and visible wavelengths," *Opt. Lett.*, vol. 42, no. 1, pp. 21–24, Jan. 2017, doi: 10.1364/OL.42.000021.

[8] K. V. Acoleyen, W. Bogaerts, and R. Baets, "Two-dimensional dispersive off-chip beam scanner fabricated on silicon-on-insulator," *IEEE Photon. Technol. Lett.*, vol. 23, no. 17, pp. 1270–1272, Sep. 2011, doi: 10.1109/LPT.2011.2159785.

[9] A. Rahim et al., "Expanding the silicon photonics portfolio with silicon nitride photonic integrated circuits," *J. Lightw. Technol.*, vol. 35, no. 4, pp. 639–649, Feb. 2017, doi: 10.1109/JLT.2016.2617624.

[10] K. Ikeda, R. E. Saperstein, N. Alic, and Y. Fainman, "Thermal and Kerr nonlinear properties of plasma-deposited silicon nitride/silicon dioxide waveguides," *Opt. Exp.*, vol. 16, no. 16, pp. 12987–12994, Aug. 2008, doi: 10.1364/OE.16.012987.

[11] Q. Lin, O. J. Painter, and G. P. Agrawal, "Nonlinear optical phenomena in silicon waveguides: Modeling and applications," *Opt. Exp.*, vol. 15, no. 25, pp. 16604–16644, Dec. 2007, doi: 10.1364/OE.15.016604.

[12] S. Lin, Y. Chen, and Z. Wong, "High-performance optical beam steering with nanophotonics," *Nanophotonics*, vol. 11, no. 11, pp. 2617–2638, May 2022, doi: 10.1515/nanoph-2021-0805.

[13] Q. Wang, S. Wang, L. Jia, Y. Cai, W. Yue, and M. Yu, "Silicon nitride assisted 1×64 optical phased array based on a SOI platform," *Opt. Exp.*, vol. 29, no. 7, pp. 10509–10517, Mar. 2021, doi: 10.1364/OE.420921.

[14] S. Sabouri and K. Jamshidi, "Design considerations of silicon nitride optical phased array for visible light communications," *IEEE J. Sel. Topics Quantum Electron.*, vol. 24, no. 6, Nov./Dec. 2018, Art. no. 8300707, doi: 10.1109/JSTQE.2018.2836991.

[15] N. A. Tyler et al., "SIN integrated optical phased arrays for two-dimensional beam steering at a single near-infrared wavelength," *Opt. Exp.*, vol. 27, no. 4, pp. 5851–5858, Feb. 2019, doi: 10.1364/OE.27.005851.

[16] C. S. Im et al., "Backward-emitting silicon nitride optical phased array enabling efficient wavelength-tuned beam steering," *IEEE Photon. J.*, vol. 12, no. 5, Oct. 2020, Art. no. 6601910, doi: 10.1109/jphot.2020.3019060.

[17] Z. Du, T. Fu, M. Chen, S. Yang, and H. Chen, "Silicon nitride integrated two-dimensional wavelength tuning optical phased array," in *Proc. 7th Symp. Novel Photoelectronic Detection Technol. Appl.*, 2020, Art. no. 1176380.

[18] S. Romero-García, F. Merget, F. Zhong, H. Finkelstein, and J. Witzens, "Silicon nitride CMOS-compatible platform for integrated photonics applications at visible wavelengths," *Opt. Exp.*, vol. 21, no. 12, pp. 14036–14046, Jun. 2013, doi: 10.1364/OE.21.014036.

[19] Q. Wang et al., "Dual-layer waveguide grating antenna with high directionality for optical phased arrays," *Appl. Opt.*, vol. 58, no. 21, pp. 5807–5811, Jul. 2019, doi: 10.1364/AO.58.005807.

[20] T. Chan, E. Myslivets, and J. E. Ford, "2-dimensional beamsteering using dispersive deflectors and wavelength tuning," *Opt. Exp.*, vol. 16, no. 19, pp. 14617–14628, Sep. 2008, doi: 10.1364/OE.16.014617.

[21] T. Komljenovic, R. Helkey, L. Coldren, and J. E. Bowers, "Sparse aperiodic arrays for optical beam forming and LiDAR," *Opt. Exp.*, vol. 25, no. 3, pp. 2511–2528, Feb. 2017, doi: 10.1364/OE.25.002511.

[22] R. Fatemi, A. Khachaturian, and A. Hajimiri, "Nonuniform sparse 2-D large-FOV optical phased array with a low-power PWM drive," *IEEE J. Solid-State Circuits*, vol. 54, no. 5, pp. 1200–1215, May 2019, doi: 10.1109/JSSC.2019.2896767.

[23] L.-X. Zhang et al., "Large-scale integrated multi-lines optical phased array chip," *IEEE Photon. J.*, vol. 12, no. 4, Aug. 2020, Art. no. 6601208, doi: 10.1109/JPHOT.2020.3001005.

[24] W. Chang et al., "Inverse design and demonstration of an ultracompact broadband dual-mode 3 dB power splitter," *Opt. Exp.*, vol. 26, no. 18, pp. 24135–24144, Sep. 2018, doi: 10.1364/OE.26.024135.

[25] Q. Lu et al., "High-speed ultra-compact all-optical NOT and AND logic gates designed by a multi-objective particle swarm optimized method," *Opt. Laser Technol.*, vol. 116, pp. 322–327, Aug. 2019, doi: 10.1016/j.optlastec.2019.03.032.

[26] M. Meem et al., "Large-area, high-numerical-aperture multi-level diffractive lens via inverse design," *Optica*, vol. 7, no. 10, pp. 252–253, Oct. 2020, doi: 10.1364/OPTICA.408579.

[27] L. Lu et al., "Inverse-designed ultra-compact star-crossings based on PhC-like subwavelength structures for optical intercross connect," *Opt. Exp.*, vol. 25, no. 15, pp. 18355–18364, Jul. 2017, doi: 10.1364/OE.25.018355.

[28] B. Shen, P. Wang, R. Polson, and R. Menon, "An integrated-nanophotonics polarization beamsplitter with 2.4×2.4 μm^2 footprint," *Nature Photon.*, vol. 9, no. 6, pp. 378–382, Jun. 2015, doi: 10.1038/NPHOTON.2015.80.

[29] A. F. Oskooi, D. Roundy, M. Ibanescu, P. Bermel, J. D. Joannopoulos, and S. G. Johnson, "Meep: A flexible free-software package for electromagnetic simulations by the FDTD method," *Comput. Phys. Commun.*, vol. 181, no. 3, pp. 687–702, Mar. 2010, doi: 10.1016/j.cpc.2009.11.008.

[30] N. A. Tyler et al., "SiN integrated photonics for near-infrared LiDAR," in *Proc. IEEE Compon., Packag., Manuf. Technol. Symp. Jpn.*, 2018, pp. 63–66.

[31] M. J. R. Heck, "Highly integrated optical phased arrays: Photonic integrated circuits for optical beam shaping and beam steering," *Nanophotonics*, vol. 6, no. 1, pp. 93–107, Jan. 2017, doi: 10.1515/nanoph-2015-0152.

[32] P. Ma et al., "Unidirectional SiN antenna based on dual-layer gratings for LiDAR with optical phased array," *Opt. Commun.*, vol. 501, Dec. 2021, Art. no. 127361, doi: 10.1016/j.optcom.2021.127361.